# Maximizing Spontaneous Jet Density and Nanofiber Quality in Unconfined Electrospinning: The Role of Interjet Interactions

Michael P. Roman,[†] Nagarajan M. Thoppey,[‡] Russell E. Gorga,[‡] Jason R. Bochinski,[†] and Laura I. Clarke*,[†]

[†]Department of Physics, North Carolina State University, Raleigh, North Carolina 27695, United States
[‡]Fiber and Polymer Science Program, North Carolina State University, Raleigh, North Carolina 27695, United States

ABSTRACT: The interplay between an applied electric field and fluid properties was studied for a polymer solution forming high quality nanofibers via electrospinning. Unconfined electrospinning—in which a fluid thin film or bath exposed to an electric field spontaneously generates many parallel fiber-forming jets—is a practical approach to achieving a high fabrication rate of quality nanofibers as compared to traditional single-needle electrospinning. The density of fiber-forming jets is controlled by surface tension effects at the lowest applied voltages but by jet-to-jet interactions as the voltage amplitude is increased, resulting in an intermediate operating voltage level at which jet number is maximized. This general result is applicable to electric-field-driven fluid instabilities in a wide range of systems. The optimal voltage level occurs when interjet interactions begin to solely determine the characteristic jet spacing, and in this regime, compression of the cone-jet slightly chokes the feed rate, allowing high quality fibers to be formed when the maximum number of jets is present. Spontaneous jet deflection (here, from a linearly arranged source) results in a two-dimensional array at the collector which both minimizes interjet interactions and preserves fiber quality.
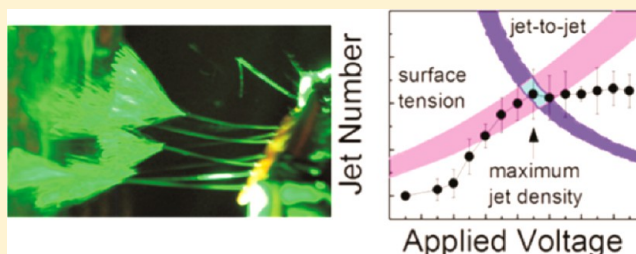
1. INTRODUCTION

Polymeric nanofibers are highly desirable for technological applications[1] with large societal impact, including air and water filtration,[2−5] energy storage,[6,7] catalysis,[8] and a multitude of biomedical uses,[9] such as controlled drug delivery,[10−12] wound healing,[13] and artificial tissue engineering.[14,15] The large surface-area-to-volume ratio, the high porosity of nanofiber collections, the similarity between the nanofiber shape and size and structures found in natural biological systems (e.g., extracellular matrices upon which cells organize into tissues in mammals), and the ability to transform polymeric precursors into carbon or ceramic nanofibers[16] are specific attributes that make these nanomaterials broadly useful, both in neat form and as fillers for composite systems.[17]

Electrospinning is a well-established, inexpensive technique for nanofiber fabrication,[18] which in its traditional form (where production relies on externally controlled fluid flow through a single-needle orifice) is plagued by low throughput.[19−22] Over the past 5 years, there has been great interest in electrospinning in unconfined geometries; one example of such a system is "edge" electrospinning from a thin sheet of polymer fluid on some solid surface. The unconfined spinning approach is particularly powerful as the process spontaneously generates and organizes many fiber-forming jets, resulting in significant gains in material throughput while maintaining high fiber quality via clever strategies to control the polymer solution feed rate (for instance, appropriate manipulation of the applied electric field[21]); additionally, there are no nozzles to clog or

complex moving parts, and the system can be indefinitely refreshed (i.e., operate either as a single batch feed or under continuous production). Avoiding gravity-driven flow (by instead exclusively utilizing an electric field control approach) further enables continuous tuning of flow rate and limit of feed to a range where high quality fiber formation is possible, as high feed rates are associated with thick and thus undesirable nanofibers. Such approaches are likely the most commercially viable for scaled-up nanofiber production and with control of fiber diameter could allow for inexpensive fabrication of large quantities of high quality nanofibers. Furthermore, in the unconfined electrospinning process, interesting physics comes into play, as the electric field and the various attributes of the fluid interact to control the number of fiber-forming (jet) sites and the mass flow through each jet.[22] It is exactly this fundamental science that must be understood to appropriately control the unconfined electrospinning process to achieve the desired production rate and quality to address both current and future application needs.

Although several reports on electrospinning in unconfined geometries[20−31] now exist, there is still a lack of a systematic discussion of the underlying physics, particularly when varying the fluid properties and/or electric field conditions under which fibers are formed. In addition, far more theoretical works on
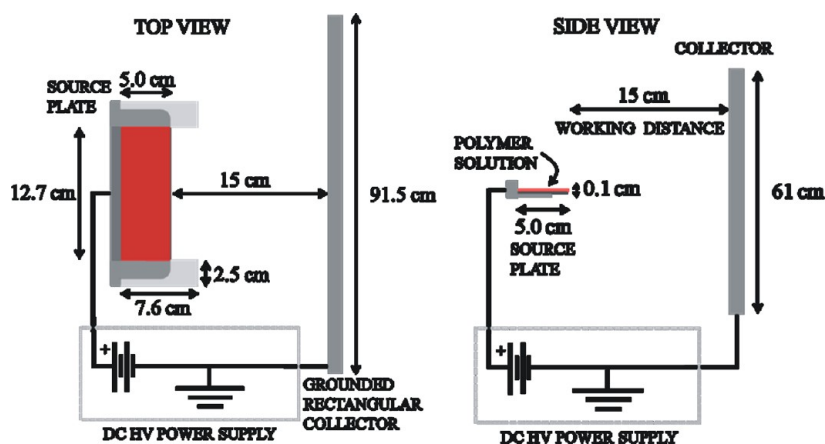
Figure 1. Schematic of flat plate, edge electrospinning apparatus. A uniform thin layer of polymer fluid coats a horizontally oriented metal plate held at positive-polarity high voltage. The source plate outer corners are rounded to prevent discharge; glass guides attached to the top surface of the plate define the borders of the electrospinning region along the front edge. A grounded rectangular collector is arranged orthogonal to the source plate at a fixed working distance.

electric field−fluid interactions have appeared than corresponding experimental reports.[32] Here, by utilizing a particularly simple experimental configuration (i.e., polymer fluid at the edge of a horizontally oriented metal plate), direct comparison between the existing theories with real-life, technologically relevant situations can be made; such evaluation reveals that different physical constraints are at play as the voltage levels are changed. For instance, jet-to-jet interactions are important in any approach with high spatial jet density from massive multineedle arrays to high throughput unconfined electrospinning, but there are very few quantitative discussions of jet-to-jet effects in the literature. Here, we find that jet-to-jet interactions limit jet number at high voltage levels instead of the usual surface tension effects. In fact, such a quantitative prediction of electrostatic repulsion between protrusions is important for any system that undergoes spontaneous fluid fingering under the presence of an electric force.[32]

We observe protrusion (jet) number, throughput per jet, and fiber quality over a large applied voltage range for solutions of different viscosity when electrospinning from a fluid-covered flat plate. Observed deviations from theoretical predictions occur both at low applied voltage (where the jet number falls off more sharply than expected) and at high voltage amplitude (where the jet number saturates), which is attributed to jet-to-jet interactions. We discuss a systematic study of cone-jet (meniscus) diameter for single jets as a function of applied voltage and fluid viscosity, compared with cone size when many jets are present, and correlate the observed cone size with fluid throughput per jet. Electrostatic interjet interactions are confirmed by a simple theoretical model in conjunction with synergistic experiments which observe a decrease in jet stability, an inability to increase the jet number with increased voltage, a suppressed cone-jet size, and splaying of the jets away from the shortest distance from fluid to collector. Importantly, we demonstrate that jet-to-jet interactions provide a benefit in unconfined electrospinning, limiting flow rate at high voltages, which preserves fiber quality. The manipulation of jet-to-jet interactions provides a useful tool to control flow rate (and thus maintain nanofiber quality) when electrospinning in an unconfined geometry.

2. EXPERIMENTAL SECTION

2.1. Materials and Solution Characterization. Experiments were performed using poly(ethylene oxide) (PEO) (400 kg/mol, Scientific Polymer Products) dissolved in deionized (18 MΩ·cm) water to create either 4 or 6 wt % polymer solutions. Solutions were typically stirred for 24 h at room temperature prior to use in order to aid dissolution. A trace amount of rhodamine 590 chloride (R6G) (479 g/mol, Exciton) was added to the solutions (0.000 05 wt %) in order to enhance video and still image capture of the process for analysis. All materials were used as received.

Solution zero shear viscosity was measured with a stress-controlled rheometer (REOLOGICA Instruments AB, StressTech) having a parallel plate geometry (45 mm diameter and a plate gap of 0.4 mm), over a stress range which was varied from 1 to 300 Pa using 23 increments, resulting in a shear rate range from 0.1 to 300 1/s. The zero shear viscosity was calculated to be 1.07 ± 0.05 and 7.46 ± 0.37 Pa·s for 4 and 6 wt % solutions, respectively. Solution surface tension was evaluated using the Wilhelmy-plate method by a surface tensiometer (Future Digital Scientific Corp, DCAT11), giving a concentration independent value of 60.0 ± 1.4 mN/m. All solution characterizations took place at 25 °C.

2.2. Electrospinning Apparatus and Procedure. Nanofibers were fabricated with an experimental setup consisting of three main elements as shown in Figure 1: the source plate, the collector plate, and the power source. The source plate, $16.5 \times 5.0 \times 0.025$ cm (length × width × thickness), was made from commercially available aluminum flashing cut to size, flattened, and cleaned for 30 min via an ultraviolet-ozone system (Novoscan PSD-UV). The plate corners were rounded (to a radius of curvature of 1.5 cm) and polished smooth by hand in order to reduce discharging. Two glass microscope slides, $2.54 \times 7.62 \times 0.1$ cm (Fischer Scientific), were adhered flat near the edges of the source plate, 12.7 cm apart (inside to inside edge), in order to prevent asymmetric jet migration to the plate ends. As schematically shown in Figure 1, each glass slide overhung the edges of the source plate by 0.635 cm (in the length dimension, perpendicular to the plate-collector direction) and 2.6 cm (in the width dimension, perpendicular to the plate edge, along the plate-collector direction). To increase mechanical rigidity, the thin source plate was mounted on a thicker aluminum base plate (0.25 cm), while overhanging past the base plate by 1.125 cm in order to maintain the proper front edge high field strength for electrospinning. The entire source plate setup was mounted on an electrically isolated adjustable stage and aligned so that the plate edge was parallel to the collector and placed at a working distance d of 15 cm (plate edge to collector). Relative to horizontal, electrospinning was possible under a variety of different plate angle orientations; however, for maximum control of the jet feeding process,

a purely horizontal orientation (0 ± 1°) provided the best results and was used for data presented in this work.

The collector, a commercially available aluminum sheet 61.0 × 91.5 × 0.1 cm (height × width × thickness), was mounted on a home-built, insulated, horizontally translatable stage and attached to electrical ground. Preweighed aluminum foil was attached to the collector surface in order to capture the electrospun nanofiber mats for mass throughput and scanning electron microscopy (SEM) analysis. The positive-polarity voltage source (Glassman High Voltage, Model FC60R2) was electrically connected to the back of the source plate.

Polymer solution was typically applied directly to the source plate (while at ground potential) using a syringe with the glass slides and back of the plate acting as raised barriers to guide and contain the fluid. Excess solution was removed with a straight edge to ensure an initial flat smooth film (0.9 ± 0.05 mm) with uniform coating near the plate edge. Reproducibility of the electrospinning process was greatly enhanced by ensuring that the plate edge was fully wetted and the fluid thickness was uniform across the spinning edge of the plate. The fluid level on the plate was actively monitored and did not significantly reduce during a typical 10 min experimental time window. While polymer fluid can be continuously replenished during electrospinning via a precision metering syringe-pump system, the results reported here are from single-batch experiments.

In order to visualize the cone-jet (meniscus) at the fluid edge, the resulting expelled fluid jet, and the forming fiber in the spatial region between source plate and collector, the working area was fully illuminated with an expanded, retro-reflected 532 nm, 150 mW green diode laser. This provided sufficient illumination for both high definition, time-stamped video (Panasonic HDC-TM80) and still image capture (Nikon D40 with AF-S Nikkor 18−55 mm lens) of multiple jets: for higher spatial resolution, a second camcorder (Sony, Model DCR-SR68) with a T monocular lens (Zeiss, 6 mm × 18 mm) provided enhanced viewing for jet analysis.

As described in previous work,[21,22] a two-stage applied voltage process was utilized to first generate a large number of jets (at an initiating, high voltage level) and then the driving force (voltage) was reduced to set an appropriate flow rate for high quality fiber fabrication. At the lower (so-called "working") voltage level, surviving jets are quasi-stable, but new jets cannot be formed. For the current report, 60 kV was applied to the source plate until the spontaneous initiation of a single jet, followed by rapid expansion of the jet population across the entire plate, plus an additional 3−5 s wait time to allow the jets to organize and stabilize. The voltage was then manually reduced to the desired steady-state working voltage level (13−28 kV) in a smooth manner over a 5−8 s time frame (i.e., at a rate ~5−10 kV/s). (Note: if a more rapid voltage level decrease was employed, it detrimentally resulted in unnecessary additional loss of jets.) After reaching the working voltage amplitude, the collector was laterally shifted to spatially separate the region for collection of high quality fibers from the polymer fluid which accumulated directly onto the collector during the initiation process. The working voltage level was kept constant for the remaining duration of the experiment. For the single jet experiments, solo jets were created by intentionally rapidly reducing to a nonoptimal initial low applied voltage; once a solitary jet was established, the voltage level was subsequently adjusted to whatever experimentally desired working value.

2.3. Analysis and Fiber Characterization. Maximum jet number and jet number versus time were determined through video analysis (Panasonic HDC-TM80). Jet diameter analysis (ImageJ Analyzer) utilized still images from videos (Sony, Model DCR-SR68 using a 6 mm × 18 mm Zeiss T monocular lens) of a magnified region of the plate edge. Mass throughput calculations were performed by weighing the foil collection sheets before and after electrospinning for 10 min at the working voltage (after allowing for a minimum 3 h drying time) and calculating the number of jet-minutes (the total number of jets multiplied by the jet lifetime in minutes) from video analysis. This data were then converted into microliters per jet per minute by utilizing the known solution concentration and PEO density of 1.21 g/cm^3.[33] Electric field modeling was performed using Maxwell 3D software (ANSOFT Corporation).

Nanofiber morphology was visualized using a scanning electron microscope (SEM, FEI Phenom-World BV) operating at 5.0 kV. Samples were sputter-coated (QuoronTechnologies, S67620) with ~100 Å Au−Pd in order to reduce charging and create a conductive surface. SEM images were analyzed (ImageJ Analyzer) to determine fiber diameter and mat porosity. Twenty-five individual fiber diameter measurements (per image at 10000× magnification) were taken in order to compute the characteristic mean and standard deviation of the fibers. Mat sample porosity was calculated using previously verified approach[34−41] by adjusting the grayscale to identify the top layer of fibers and quantify the number of filled (top layer) and unfilled (remainder) pixels in each image.

3. RESULTS

3.1. Single Jet Cone-Jet Diameter versus Voltage. We begin by examining the characteristics of single jets, so that the solo jet behavior can be compared with situations where many jets are present and thus when interjet interactions potentially occur. Whenever any perturbation to the surface of a fluid arises, there is a characteristic size scale over which the disturbance relaxes (for instance, the meniscus that forms when a fluid encounters a wall). In unconfined electrospinning, the fluid perturbations at the plate edge are initially a spontaneous fingering of fluid under the driving influence of the electric field (akin to the distinctive pattern of droplets that forms when wet paint drips from a ceiling under the influence of gravity), as discussed in more detail in section 3.2. With time, these fingers evolve into emitting cone-jets, where the velocity of the fluid is the highest at the jet apex and the fluid is unperturbed far from the cone-jet. The term cone-jet is utilized in literature to indicate that the largest velocity occurs in a relatively narrow "jet" region surrounded by a larger perturbation (the cone) that is more stationary.[42] In Figure 2, the diameter of the cone-jet (at the plate edge where it has its maximum width) for single, isolated jets, as a function of applied voltage is presented for solutions of differing viscosity, where black squares (open gray circles) depict results for a 4 wt % (6 wt %) solution.

Physical insight into this experimental situation can be gained by utilizing a common simplifying approach for viscous fluid
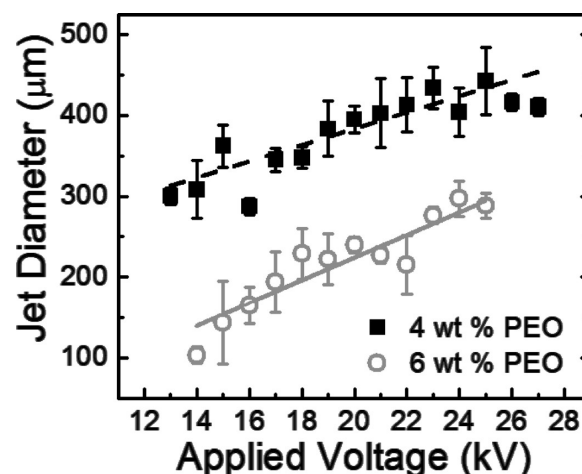

Figure 2. Cone-jet diameter measured at the plate edge for single jets formed from 4 wt % (black squares) or 6 wt % (open gray circles) PEO solutions (initial film thickness 0.9 ± 0.05 mm) as a function of the source plate applied voltage level. The dashed black line (4 wt % PEO) and solid gray line (6 wt % PEO) are linear fits to the data points. Error bars represent the statistical distribution from 3 to 5 separate experiments.

flow: assuming a driving force in one direction which sets up a velocity gradient in a perpendicular dimension (i.e., the lubrication approximation[43]). The effect of viscosity in general is that velocity changes cannot be instantaneous and, rather, must occur over a finite length scale. In this case, the electric field creates the driving force (along x, the plate-collection direction) which generates a velocity (v) gradient along the plate (z direction) which results in the cone-jet. Because the system is viscous, it quickly reaches steady state where the driving and viscoelastic forces (per volume) balance. In this approach

$$\left|\frac{dP}{dx}\right| = \left|\eta\frac{d^2v}{dz^2}\right| = \varepsilon_0 E\left|\frac{\partial E}{\partial x}\right| \cong \frac{\eta\bar{v}}{3a^2} \tag{1}$$

where P is the pressure (here the electrostatic pressure $P = {}^1/_2\varepsilon_0 E^2$ with E the electric field) and η is the viscosity. The viscoelastic force pulls back against and balances the force due to the gradient in pressure. As shown in the latter portion of eq 1, due to the parabolic nature of the velocity gradient (as easily seen by solving the eq 1 for $v(z)$), a simple form relating the average velocity ($\bar{v}$) and the characteristic distance over which velocity drops to zero (here, the cone radius, a) can be generated.[43] It is important to realize that many of the parameters in eq 1 are inter-related. Naively solving this equation for a^2 would give the impression that as the applied voltage (and thus the electric field strength and gradient $|\partial E/\partial x|$) increase, the jet size should decrease. However, this result is incorrect (as demonstrated by the data in Figure 2) because as the voltage increases, the maximum and average fluid velocity also increase, leading to a net increase in cone-jet size. Similarly, for a decreased viscosity (such as transitioning between the two different solutions in Figure 2) one might expect a decrease in cone-jet size, but again, a decreased viscosity also results in an increase in velocity, which is the dominant effect. We conclude that the velocity is the dominant factor in determining the cone-jet diameter in this experimental regime. In Figure 2 and eq 1, as the driving force increases, both the velocity and the cone-jet diameter increase, with the latter resulting from the longer length scale needed to transition from the maximum to zero velocity.

The assertion that the velocity and flow rate increase dramatically with applied voltage in the single jet case is consistent with experimental observations of the fluid in the fiber forming region (between source plate and collector). Figure 3 shows a characteristic image of the fluid path from source plate to collector, appropriately depicting the experiment (and the electrospinning process[18] in general) during most applied working voltage conditions. The collector is out of view in the foreground below the bottom of the image. The R6G-tinted polymer solution on the source plate appears orange-colored in the image. In the fiber forming region, the jets strongly scatter the green laser light used for illumination. In particular, the fluid initially travels on a straight-line path (generally referred to as the linear region) toward the collector. Note: the forming fiber in the linear region is slightly out of focus in the image. As the fluid stream/forming fiber thins (due in part to evaporation of solvent and stretching of the protofiber), the elongated charged fiber become electrostatically unstable and begins to whip or bend (the whipping region) due to intrafiber charge interactions. This whipping process dramatically thins the fiber, resulting in dry nanofibers arriving at the collector plate.[18] In general, as the flow rate
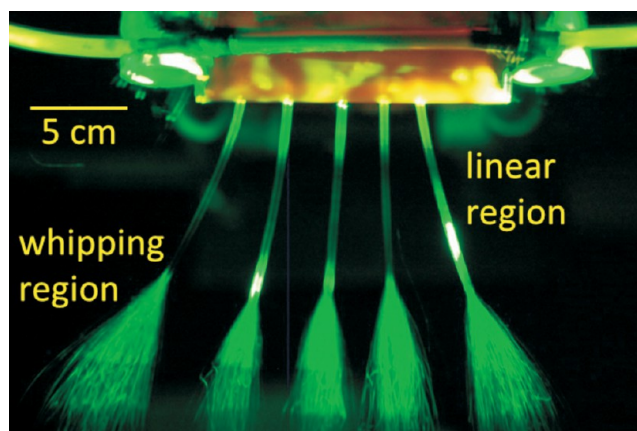
Figure 3. Characteristic image of multiple parallel electrospinning jets formed at the edge of a fluid-covered conducting source plate (top of image) and the resultant linear and whipping regions of the jets. The electrospinning process begins with a linear region, where a thin stream of fluid moves along a straight line to the collector. After the moving fluid stream thins sufficiently, electrostatic forces within the charged fiber result in a whipping instability, seen here as the superposition of many different positions (due to the fast, chaotic fiber motions during the image exposure time) shown as the in-focus, brush-like structure at the bottom of the picture. Note: for ease of viewing, the glass guides at the plate corners were removed for this image.

increases, the length of the linear region extends (with a corresponding decrease in whipping), and at very high flow rates, fiber formation is not possible as the fluid volume is too large to allow formation of the whipping instability and wet fluid is transported directly from the source to the collector (a detrimental process referred to as "streaming"). In the single jet experiments, we observed a normal electrospinning process with linear and whipping regions for applied voltages less than ~19 kV for the lower viscosity 4 wt % solution and at less than ~22 kV for the higher viscosity 6 wt % solution. At higher working voltages, overt streaming occurred, indicating high flow rates. This observation is consistent with the throughput analysis in section 3.4 and also occurred in multijet cases (see section 3.2) at high applied voltage levels when the jet number dropped and previous fiber-forming jets expanded in size and began to stream the wet fluid.

Based on the analysis of eq 1, an estimate of the characteristic cone-jet size for a particular fluid and applied electric field can be determined if a characteristic average velocity is known. Previously, we proposed that the electrospinning process in edge electrospinning (e.g., electrospinning from a fluid near a sharp edge) was directly analogous to traditional needle electrospinning (i.e., pumping polymer fluid through a needle as a source) in cases where the electric field, electric field gradient, and flow rate were similar.[20−22] Thus, the fluid experienced comparable forces and formed fibers of similar average diameter and diameter distribution in superficially different systems. In fact, in needle electrospinning of the 6 wt % solution, a flow rate of 5 μL/min through a 20 gauge needle (inner diameter 0.603 mm) results in fibers of 246 ± 21 nm, which overlaps the average fiber diameter from the same solution in the current plate configuration over a wide voltage range. In particular, at 18 kV, the measured (plate) fiber diameter is 250 ± 25 nm, and the electric field and electric field gradient match well with that found in the traditional needle case. In addition, throughput measurements from the plate

configuration (for multiple jet experiments) confirm that the volume per jet from 14 to 20 kV is ~6 μL/min. Thus, from the needle flow rate and size, an average characteristic fluid velocity of 2.9×10^{-4} m/s can be determined. Using this value in eq 1, along with the known electric field (2.3×10^6 V/m) and field gradient (1.5×10^9 V/m^2) (both from simulations), and viscosity (7.46 Pa·s), yields a characteristic cone-jet diameter of ca. 300 μm, which is consistent with the data in Figure 2. This is an overestimate of cone-jet size as the fluid viscosity will be lower at the nonzero shear rate within the jet. One can estimate this effect from the measured rheological viscosity versus shear rate curve, estimating the shear rate as v divided by the experimentally measured cone-jet radius (the distance over which the velocity drops to zero). From the data in Figure 2 (d = 229 μm at 18 kV), we obtain a shear rate of 2.5 1/s. At this shear rate, the viscosity has dropped to approximately 6 Pa·s, which yields an estimated cone-jet diameter of 270 μm.

As a final note, generally meniscus sizes are determined by surface-tension effects and in particular the appropriate capillarity length (when the perturbation size is greater than the characteristic capillarity length in the system) or by the size of the perturbation (for instance, the fiber size when dipping a solid fiber into a fluid) if smaller than the capillarity length.[43] The capillarity length κ^{-1} is related to the ratio of the surface tension to the important driving force per volume. For gravity-driven processes $\kappa_g^{-1} = (\gamma/\rho g)^{1/2}$ = 2.5 mm for our case, where γ is the surface tension, ρ is the density of the fluid (here dominated by the water solvent), and g is 9.8 m/s^2. For perturbations smaller in size than this characteristic length scale, effects due to gravity are negligible. (Gravity is also negligible due to the horizontal configuration of our plate.) The important capillarity length in our system is related to the electrostatic driving force, $\kappa^{-1} = [\gamma/(\varepsilon_0 E|\partial E/\partial x|)]^{1/2}$ = 1.4 mm at the working voltage and 420 μm during the initiation stage. These values have consequence in determining the number of jets (section 3.2) but not in directly controlling the cone-jet width (with a much smaller characteristic size of ~150 μm) in the working voltage regime, which is dominated by the fluid velocity/flow rate. When the system is driven more strongly (which is not appropriate for high quality fiber formation), the velocity will approach the "characteristic" fluid velocity, $\bar{v} = \gamma/\eta$, which when incorporated into eq 1 gives $a = \kappa^{-1}$, to within a numerical constant on the order of 1. Thus, when the system is driven more strongly, surface tension effects are important and seamlessly take over. The relatively unusual direct dependence of jet width on velocity is due to this specialized, critical application of nanofiber formation which requires operation in the weak driving regime that is generally less discussed in prior literature.

3.2. Jet Number versus Voltage. Figure 4 summarizes the maximum jet number versus applied voltage for a 6 wt % solution of PEO (i.e., the higher viscosity solution). In contrast with model predictions (discussed below) that rely solely on the interaction between surface tension and electric field (in other words, that neglect jet-to-jet interactions), instead of a monotonically increasing jet number with voltage, the maximum jet number saturates. Whereas the filled black circles in Figure 4 are the maximum jet number (observed within 1 min of stabilizing at the working voltage level), the open gray circles are the average jet number present over a 10 min experiment. As can be seen, above this saturation voltage, jet stability also decreases as exemplified by a lower average number of jets. This observation indicates that jet-to-jet
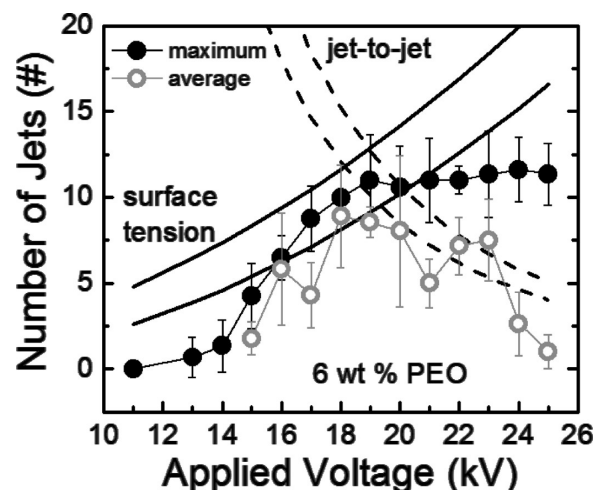
Figure 4. Maximum (black circles; measured within 1 min of reduction to working voltage) and average (open gray circles; over a 10 min experiment) number of stable jets as a function of working voltage for a 6 wt % PEO solution. The solid lines represent the expected jet number if the spacing between jets (λ) is determined solely by the interplay with surface tension (eq 2). The range reflects reasonable uncertainty in the exact electric field value (the pertinent value will be between the plate edge and the terminus of the cone-jet) and the uncertainty in the electric field simulation. The dotted lines represent the limit on jet number due to jet-to-jet interactions utilizing a linear fit to the natural single jet cone widths in Figure 2 and eq 4, as discussed in the text. The range reflects the average measurement error in the cone-jet width.

interactions are important. We first examine known models that predict jet number (neglecting electrostatic jet-to-jet interactions) and show that these overlap the observed jet number prior to saturation.

As discussed in a previous publication,[22] there is a direct analogy between the formation of fluid protrusions (ultimately, jets) in the process of electrospinning from an unconfined polymer fluid film and the traditional Rayleigh–Taylor instability (driven by gravity and commonly observed as droplet formation in a thin film of wet paint on a ceiling). Utilizing this analogy and the published treatment by de Gennes,[43] a simple model can be generated to estimate λ the average spacing between protrusion/jet sites where the fluid fingering process relies on flow of fluid along the plate toward forming protrusions. By estimating the flow rate ($Q \approx h\tilde{v}$ where h is the film thickness and $\tilde{v}$ the average velocity along the plate given by $\tilde{v} \approx (h^2/3\eta)(\partial P/\partial z)$, where z is the direction along the plate and P the pressure due to both the electric field and surface tension), utilizing a continuity equation $|\partial Q/\partial z| = |d\xi/dt|$, and assuming a simple form for the edge of the fluid surface $\xi \approx \xi_0 + \Delta\xi \cos(kz)$ with $\Delta\xi = \Delta\xi_0 e^{-t/\tau}$, one can establish a dispersion relationship between $1/\tau$ (the perturbation growth rate) and $k = 2\pi/\lambda$ (see previous work[22] for more details).

The gradient ($\partial/\partial z$) in the surface-tension pressure (or the force per fluid volume) is $\gamma(\partial^3\xi/\partial z^3)$, which is proportional to $\gamma k^3 \Delta\xi$. The gradient in the electrostatic pressure can be estimated by arguing that this pressure also oscillates as $\cos(kz)$ (with the electric field screened inside the fluid) with the amplitude of the pressure oscillation going as $\varepsilon_0 E_0^2 k \Delta\xi$, where E_0 is the average electric field $\partial\Phi/\partial x$ (Φ is the electric potential) not accounting for the effect of fluid perturbations. Because the fluid is conducting, the fluid surface is an equipotential, and the oscillating fluid results in a more rapid

change in potential (reflected in the k-dependence) and thus electric field enhancement, which results in increased pressure (as the electrostatic pressure goes in proportion to $\varepsilon_0 E^2$). Moving along a path parallel to the plate edge, the field drops from E to zero (due to the screening effect of the protruding fluid) over a distance of $\lambda/2$. Thus, the electrostatic force per volume due to the perturbed surface is proportional to $\varepsilon_0 E^2 k \Delta \xi$. In this model, an appropriate electric field (as the electric field changes moving away from the plate edge) would be an intermediate value between that found at the plate edge and that occurring at the apex of the fluid oscillations. This form for the electrostatic pressure driving force differs from the one utilized previously,[22] where the explicit gradient in the field due to the metal plate geometry was included in a different manner. We find that the current approach, focused on the fluid screening, provides a better fit to the experimental results.

The arguments in the previous paragraph lead to a dispersion relationship of the form $1/\tau \approx \gamma k^4 - \varepsilon_0 E^2 k^3$ to within numerical constants. The fastest growing oscillation (minimum $1/\tau$ versus k) will dominate, which leads to

$$\lambda = 2\pi \frac{N\gamma}{\varepsilon_0 E_0^{\ 2}} \tag{2}$$

where λ is the characteristic distance between jets, E_0 is the electric field near the plate edge (see above discussion), and N is a numerical constant. Thus, as expected from intuition, a stronger electric field allows for more jets (smaller spacing between jets λ), whereas an increase in surface tension results in a decreasing number of jets for a given plate edge size.

Equation 2 can also be obtained from a more sophisticated published analysis.[26] This approach considers both fluid coated spheres and planar liquid layers. As in the above treatment, a dispersion relation is developed that relates the rate at which perturbations grow ($\sigma = 1/\tau$) to the characteristic wavenumber ($k = 2\pi/\lambda$). To apply the theory to the current system, we began with the dispersion relation for a viscous fluid in the planar case, removed the term relating to gravity, and utilized the authors' approximations for highly viscous cases ($2k^2\eta/\rho \gg \sigma$ with ρ density) and thin films (small kh, where h is the film thickness) which results in eq 2 with $N = 2$. Alternatively, one can take the limit of the spherical case for thin liquid layer (taking the radius of the sphere, a, or $n = ka$, to infinity), leading to a dispersion relation (eq 50[26])

$$\sigma = \frac{h^2}{2\eta}[\gamma k^3 - \varepsilon_0 E^2 k^2] \tag{3}$$

which yields eq 2 with $N = 1.5$. This treatment is the most rigorous result and thus will be utilized to fit the data. Equation 3 can be obtained by balancing the electrostatic and surface tension pressures with the viscous stress at the surface, $\mu(\partial v_x/\partial x)$. In this highly viscous case, the velocity is zero at the substrate and increases quadratically with x to a maximum at $x = h$. This maximum velocity goes as σ/k, since volume is moved a distance $1/k$ in a time $1/\sigma$ as perturbations form. Utilizing this form, $v(\xi) = (\xi^2/h^2)(\sigma/k)$, eq 3 is obtained. We point out that in the geometry of this previously published report[26] the electric field is applied perpendicular to the supporting surface; however, despite this small difference, the values for λ matched well with our experimental results (see below) in the moderate voltage range prior to saturation.

Equation 2 predicts a quadratic increase in jet number (proportional to $1/\lambda$) as the electric field increases. Using

electric field values from simulations and the experimentally measured surface tension generates a theoretical prediction (solid lines, Figure 4) that matches the experimental results in the moderate voltage region. For instance, eq 2 with $N = 1.5$ predicts $\lambda = 1.05$ cm at 20 kV or a maximum of 12 jets (for the 12.7 cm available region of the plate), which matches with the experimental value of 11 ± 3 jets. The simulated electric field values used in this estimate are those calculated about 75−100 μm from the plate edge, which is consistent with the size of the initial fluid perturbations. It is important to note that the voltage range well-explained by the surface-tension-dominated models represents the majority of the usual useful working region; that is, the applied voltages that will give stable jets producing high quality fibers. Thus, the surface-tension-driven model works well over this important region. However, here we extended the experimental voltage range further to show the limits of such models.

Examining Figure 4, the experimental data deviate from the theoretical predictions at high applied voltage, where the jet number remains constant instead of increasing and at low voltages (11−14 kV) where insufficient flow through the jet leads to decreased jet stability.[22,44] (Flow through the jet helps to retain the jet-cone at the low voltages required for high quality fiber formation; all working voltages are too low to initiate new jets.[21,22]) It is noteworthy that these real-world effects (related to particular velocity, viscosity, and jet−jet electrostatic interactions) are not generally incorporated in theoretical models to predict λ (and thus maximum jet number), which depends only on the electric field and surface tension. Even with adjustment of the particular fit in Figure 4, it is clear that the experimental jet number versus voltage does not increase as a simple quadratic when looking over a sufficiently large experimental range.

3.3. Jet-to-Jet Interactions: Effect on Jet Number and Stability. During the electrospinning process, the polymer fluid is electrically charged. Thus, each protrusion exerts a repulsive electric force on its neighbors (along the plate z direction). In this work, we refer to such electrostatic forces between neighboring cone-jets at the plate edge as jet-to-jet interactions. For instance, at moderate jet densities repulsion between neighboring protrusions or jets leads to relatively even jet spacing in order to minimize the electric interactions. Previously, we modeled this electrostatic force by estimating the charge per cone-jet and calculating the electric field and force on a cone-jet due to the nearest adjoining jets.[22] This electrostatic force due to neighboring jets acts to counter the viscous force that determines the cone-jet diameter (see section 3.1) and thus tends to compress cone-jets, moving charge closer to the cone-jet apex and thus further from other cone-jets. The jet-to-jet electrostatic force increases with source plate voltage due to three effects: (1) the increased surface charge at larger applied voltage, (2) the increasing number of jets (see eq 2) as the electric field is better able to overcome the effect of surface tension, and (3) increased flow rate and thus fluid velocity which tends to widen cone-jet diameters. Thus, at sufficiently high voltage levels, electrostatic interactions will be significant, will alter the cone-jet diameter from its natural (one-jet) size, and may serve as a limit to the feed rate. For instance, Figure 5 shows experimental cone-jet diameters obtained under a constant applied voltage level (20 kV) where the jet number is intentionally varied. Note the significant decrease (to about 70% of its original value) in the cone-jet size when 8−12 jets are present. This is a similar jet number as the saturation value
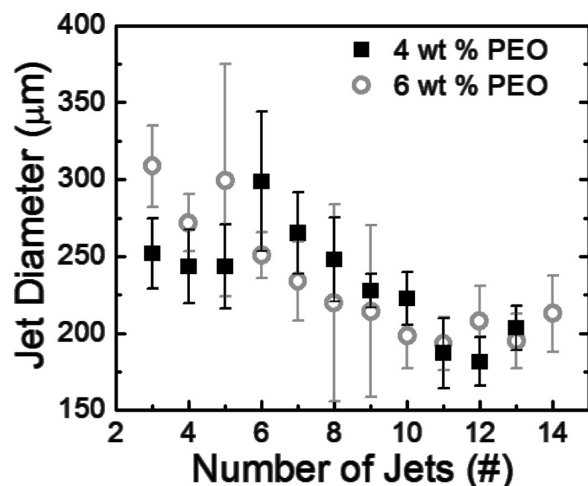
Figure 5. Cone-jet diameter measured at the plate edge under an applied working voltage of 20 kV as a function of number of jets for 4 wt % (black squares) or 6 wt % (open gray circles) PEO solutions. The error bars represent the statistical distributions from 3 to 5 separate experiments.

in the jet number versus voltage plot (Figure 4). Throughput per jet is decreased in this jet-compression range (see section 3.4).

Because compression of the cone-jet can decrease the fluid velocity, it can thereby lead to poor jet stability; hence, electrostatic jet-to-jet interactions can limit the maximum jet number. We roughly estimate a minimum λ (maximum jet number) by defining a minimum characteristic velocity required for jet stability and then setting the viscous force per volume ($\eta \bar{v}/3a^2$) equal to the electrostatic force due to neighboring jets $(1/4\pi\varepsilon_0)[\sigma^2 A^2/(\lambda - 2a)^2](2/V_{jet})$, where A and V_{jet} are the surface area and volume of a conical shaped jet and ($\lambda - 2a$) is the distance between the edges of neighboring cones. Total surface charge can be estimated from the capacitance of the plate-collector system (from computational modeling) and the known voltage. On the source plate, this charge is

predominately located on the collector facing surface of the fluid with an area of hL where $h = 0.9$ mm and $L = 12.7$ cm is the plate length. Setting the two terms above equal leads to

$$\lambda = 2a\left[1 + \sqrt{\frac{3\sigma^2 A^2}{8\pi\varepsilon_0\eta v V_{jet}}}\right]$$

(4)

From eq 4, at low surface charge density (low voltage conditions), the spacing between jets (λ) is only limited by the spatial extent of the cone-jet (the cone-jet diameter). Thus, in this regime, the fluid's surface tension (eq 2) sets the experimental limit on jet number. However, as the applied voltage level (and thus the electric field amplitude) increases, the surface tension constraint is released, whereas conversely, the limit set due to jet-to-jet interactions becomes more severe. Thus, at a sufficiently high voltage level, jet-to-jet interactions will become the dominant effect that controls the stable jet number. Using eq 4, a limiting velocity of $v = 2.9 \times 10^{-4}$ m/s and the experimentally measured jet diameter for the single jet case versus applied voltage level, the limit on jet number is plotted in Figure 4 as the dotted gray lines. Note that the two limits on jet number cross at the point where saturation in maximum jet number occurs. Thus, above this point, surface tension effects are no longer dominant, and further increases in the electric field amplitude do not produce more jets. In fact, after this point, the jet-to-jet interaction model follows the experimental data for the average jet number. Thus, at higher applied voltages, even though the initial (i.e., maximum) jet number may exceed the value predicted by the jet-to-jet interaction model, the number of *stable* jets is controlled by the jet-to-jet interaction limit.

Such analysis provides important guidance for large scale fabrication of nanofibers from unconfined electrospinning. The maximum number of stable jets will occur at the crossover between the surface tension limit (eq 2) and the limit due to electrostatic interactions between the jets (eq 4). Obtaining a higher jet density will require further electrostatic screening or manipulation of jet shape in order to mediate jet-to-jet effects. Although such a strategy can be used to maximize jet number,
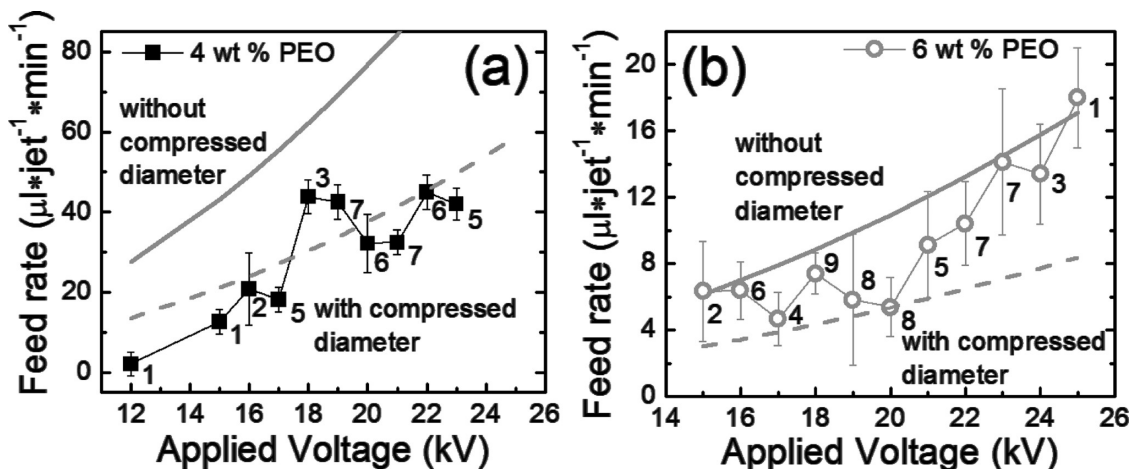

Figure 6. Feed rate per jet as a function of applied voltage for (a) 4 wt % (black squares) or (b) 6 wt % (open gray circles) PEO solutions as extrapolated from the measured mass accumulation per time. The number associated with each data point is the average number of jets during the collection time. In both graphs, the solid gray line predicts feed rate at all voltages from that measured at either 15 or 25 kV (they scale exactly) for 6 wt % solution assuming a quadratic dependence on voltage. The dotted gray line is identical but with a reduced diameter (from d to $0.7d$), assuming that the flow is quadratic in radius. For (a), the fit lines are scaled up by 7× as compared to (b), which reflects the ratio of the two different solution viscosity values.

fiber quality will still be determined by the flow rate through the jet, which needs to be sufficiently low to allow a sufficient whipping region in order to thin and dry the nanofiber. This condition may require operation at voltage levels below the maximum jet number value or, alternatively, working slightly within the jet-to-jet interaction range, where flow rate decreases due to cone-jet compression. We discuss the effect of interjet interactions on flow rate in the next section.

3.4. Jet-to-Jet Interactions: Effect on Flow Rate. Figure 6 shows experimentally measured flow rate per jet as a function of the applied source plate voltage level for the two solutions having different viscosity values. To obtain this data, the mass throughput (the mass of polymer on the collector) for a 10 min experiment is measured, the number of active jets per minute is determined from video recording, and the resultant polymer mass is converted into an equivalent solution volume using the known densities and solution concentration. Thus, this parameter is equivalent to the flow rate controlled by a syringe pump in the traditional needle electrospinning process; here the flow rate is controlled by the force due to the applied electric field. The flow rate values are per jet; in addition, the average number of jets observed during the flow rate experiment is noted next to each point. Because the connection between flow rate and the field strength is quite complex, being influenced by details of the size, shape, and velocity profile within the cone-jet as well as possible volume effects, such as the film thickness, we utilized a simple, self-consistent empirical method to fit the data, which reveals the important experimental parameters.

Simple analysis of electric-field-driven fluid motion in a variety of cases, such as that leading to eq 1, understanding of electro-osmotic flow along a surface,[43] and discussion of the fluid velocity from a drop under the influence of an electric field[44] suggest that the fluid velocity should increase in proportion to the electric field amplitude squared. From an intuitive perspective, as the applied voltage level increases, both the charge on the fluid and the electric field increase linearly; thus, the force ($F = qE$) increases as the electric field squared. If the jet diameter is relatively constant, then the results in Figure 6 should scale proportionally as the applied voltage level squared with no adjustable parameters. In fact, the solid gray line in Figure 6b utilizes the measured throughput for 15 or 25 kV (they scale exactly), adjusted by voltage squared for each point (for instance, that the flow rate goes as a^2E^2 with a constant jet diameter). Thus, points that overlap with this solid line scale as electric field squared with no adjustment for changing cone-jet diameter. However, Figure 5 indicates that at high jet number the jet diameter is suppressed to about 0.7× that at low jet number. The dotted gray line is a theoretical curve for the case where the flow rate goes as a^2E^2 and the jet diameter is constant with voltage but suppressed to 70% of that used for the solid curve. Therefore, points that overlap with this line have a compressed jet diameter. From examining the jet number values provided for each point, the flow rate values with the largest average jet number (that is, the largest number of stable jets) occur at 18–20 kV, which corresponds to the overlap point between the surface tension model prediction and the expected value due to jet-to-jet interactions in Figure 4, as discussed in the previous section. These high jet number cases also have a flow rate associated with jet compression based upon the model presented in this paragraph. The value of 8–9 jets is in fact associated with the jet compression region as shown for the 20 kV case in Figure 5.

Thus, as the jet number increases, particularly at the applied voltage levels 19 and 20 kV, the flow rate is suppressed but not to an extent that jet stability is impacted. Because of this effect, in the range 15–20 kV, the flow rate is essentially constant (Figure 6b), at a rate associated with high quality fiber formation. Observed nanofiber diameters are 230 ± 50 nm at 17 kV, 250 ± 40 nm at 19 kV, and 285 ± 30 nm at 21 kV, all values which overlap within error. Characteristic SEM images of nanofibers fabricated under multiple voltage conditions are provided in Figure 7. There is no significant difference in the
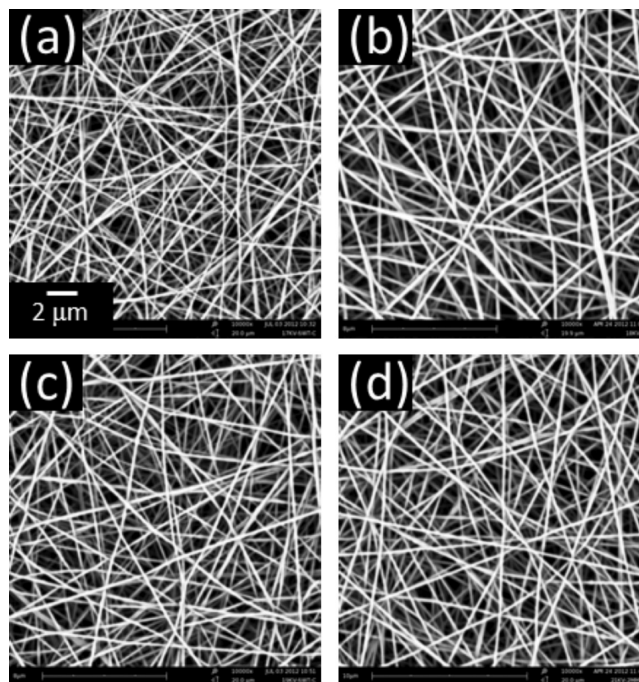
Figure 7. Characteristic SEM images of fibers produced from 6 wt % PEO solution at (a) 17, (b) 18, (c) 19, and (d) 21 kV applied voltage. The average fiber diameters are (a) 230 ± 50, (b) 250 ± 25, (c) 250 ± 40, and (d) 285 ± 30 nm. Thus, within error, both the average diameter and the diameter distribution are unchanged over this voltage range.

fiber quality. In contrast, at 22 kV, overt streaming of fluid is periodically observed (associated with flow rates >10 μL/min.) Thus, the jet-to-jet interaction effectively increases the voltage region in which high quality fibers can be fabricated, allowing one to increase the jet number without high flow rates that are inconsistent with fiber formation. At higher voltage levels above the crossover, jet compression is significant enough to decrease jet stability, and experiments of reasonable time duration show lower jet number and higher flow rate per jet (a return to the solid trend line in Figure 6b). Once the jet number is reduced—and thereby decreasing the jet-to-jet interactions effects—the flow rate subsequently increases.

Suppression of flow rate can also be observed when decreasing the fluid viscosity. Figure 6a shows flow rate as a function of the source plate applied voltage level when electrospinning from a 4 wt % PEO solution. From eq 1, a 7× increase (the factor of viscosity decrease when transitioning between 6 and 4 wt % PEO solutions) in flow rate is expected if the jet diameter and the details of the jet shape and organization stayed the same. This prediction is shown as the solid line in Figure 6a. In contrast, the dashed line shows the

7× increase but with a compressed jet diameter (70%, consistent with the dashed line in Figure 6b). Thus, the 4 wt % case has a lower flow rate over the 17−24 kV range than might be expected when multiple jets are present. This observation is consistent with the significant decrease in cone-jet diameter for the 4 wt % solution in multijet experiments (Figure 5) where, in contrast to single-jet cases (Figure 1), the cone-jet diameter is similar to that for the higher viscosity, 6 wt % PEO solution. Thus, the very wide jets (due to high velocity and flow rate) in the single-jet case are suppressed when multiple jets are present, indicating a control of flow rate under the presence of other jets. We note that the 4 wt % solution results in beaded fibers as seen previously[22] and that overt streaming of fluid was present in most 4 wt % solution experiments, consistent with high flow rates (>10 μL/min).

As alluded to above, the advantage of jet-to-jet interactions in the 19−20 kV range when electrospinning from the 6 wt % higher viscosity PEO solution is that the velocity is slightly suppressed, however not to the extent that jet stability is affected (as it clearly is, for instance, at 25−26 kV). In support of this argument, in the 4 wt % PEO solution case where the system appears to be significantly perturbed by jet-to-jet effects, jet stability does appear to be negatively impacted, as can be seen from the maximum and the average jet number values (Figure 8).
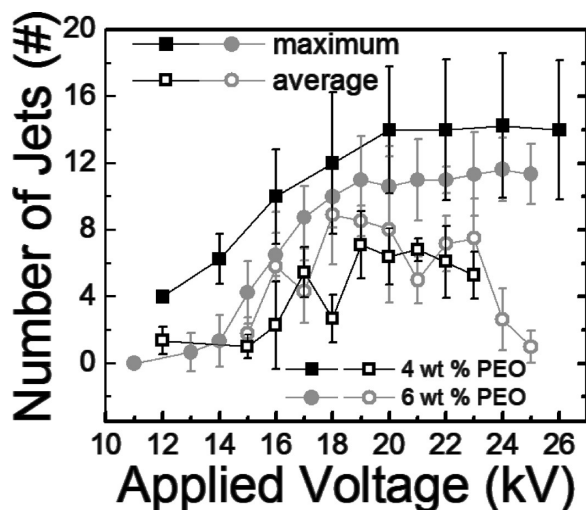

Figure 8. Maximum [(filled black squares) measured within 1 min after reduction to the working voltage level] and average number of jets [(open squares) over a 10 min experiment] as a function of the applied working voltage level for a 4 wt % PEO solution. The equivalent measurements from a 6 wt % PEO solution (filled and open gray circles, respectively) from Figure 4 are shown for comparison. Error bars reflect the statistical differences from 3 to 5 separate experimental measurements.

Figure 8 shows that the maximum jet number for the two different viscosities matches within error, as anticipated in the surface-tension-dominated regime where the maximum jet number is independent of viscosity (see eq 2). The saturation also occurs at a similar voltage and jet number values, which is consistent with the similar jet diameters and the compression of jet diameter shown in Figure 5. However, the trends in the data, particularly the larger error bars for the lower viscosity case (which reflects a wider distribution of responses over a series of identical experiments) and the greater difference between the

maximum and average jet number, indicate lower jet stability for the 4 wt % solution. Even with relatively high velocities and flow rates, which tend to preserve jets, the push−pull of a desire for high velocity and thus wider cone-jets and jet-to-jet interactions leads to a less stable system.

3.5. 1-D to 2-D Spontaneous Jet Rearrangement Due to Jet-to-Jet Interactions. As a final experimental observation, we examined the pattern of fiber deposition on the collector which provides an indication of the spacing and orientation of the jets at the plate edge. Figure 9 shows characteristic images of the high quality nanofibers accumulated on the collector when 3, 5, 7, 9, 11, and 13 jets are present (6 wt % PEO solution at 20 kV). As clearly demonstrated in the figure, when fewer than ∼6 jets are present, the jets orient directly along the shortest distance between the charged source plate and the grounded collector (i.e., the instabilities evenly space on the plate edge along the z direction and propagate directly to the collector parallel to the x direction). However, for larger jet numbers, the instabilities spontaneously rearrange themselves in order to minimize interjet interaction, consequently orienting with alternating jets perturbed and pointing slightly upward or downward (e.g., Figures 9c and 10 which directly reveals the pattern of jets) relative to the center line; that is, the jets now point with some angle in the xy-plane. For instance, at 20 kV for 11 jets, upward (downward) jets pointed 24 ± 6° (−12 ± 5°) above (below) horizontal. When the jet number grows (Figure 9d−f), the angle of deflection for neighboring jets increases, revealed as the pattern of the accumulated fibers on the collector consists of three or more rows. Larger deflection angles were observed at higher applied voltage levels. The self-driven jet deflection appears to be a useful mechanism to minimize jet interactions in the 6−9 jet range; above this, the collector patterns are less ordered and predictable. As discussed in previous sections, at >9 jets, jet-to-jet interactions are evident in terms of jet stability and flow rate. Figure 10 shows a characteristic optical image when sufficient numbers of jets are present, causing vertical deflection of their propagation directions, in contrast to the direct line path taken with small jet numbers (Figure 3).

3.6. Generality of the Edge Electrospinning Approach. Alternative approaches for scaling-up electrospinning are often hindered by poor fiber quality. Previously, we have argued that high quality fiber formation can be achieved in an unconfined geometry if the electric field is concentrated with a sharp metal feature (such as it is in needle electrospinning) and flow rate is controlled such that the unconfined fluid experiences a similar electric field and feed rate as in the traditional needle-based approach. A sharp metal edge is a particularly useful feature because fluid need only be in the vicinity of the edge for successful electrospinning. Previous work has demonstrated this approach for a flat plate exposed to small streams of fluid under gravity assisted flow[20] and for a fluid-filled bowl with a sharp lip.[21,22] In the current work, the generality of this edge electrospinning approach is further shown by simply coating a thin horizontally oriented conducting plate uniformly with polymer solution. The same underlying process occurs as observed in the bowl configuration, as detailed in previous works[21,22] and section 2.2. In fact, when electrospinning with the same characteristic polymer fluid (6 wt % PEO in water), the experimentally observed optimal parameters in the three configurations (needle, plate, and bowl) match. The electric field at the jet location is approximately 2−3 × 10^6 V/m (from simulations of each
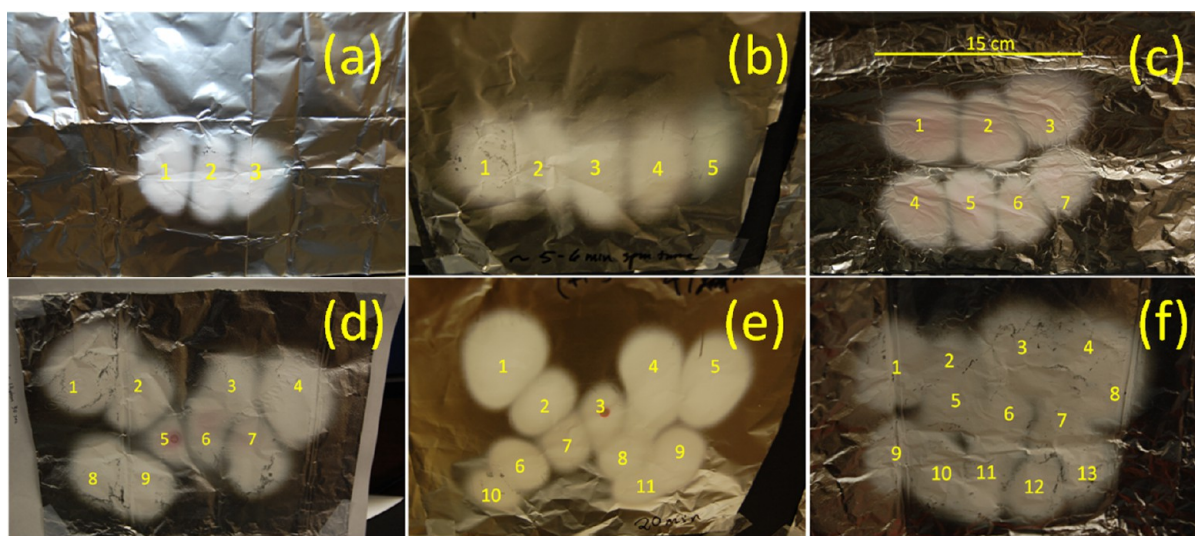
Figure 9. Pattern of nanofiber deposition on the collector plate reflects the presence of jet-to-jet interactions. Regions of nanofiber depositions are lighter in color on the aluminum foil covering the collector. The observed jet number at the plate edge matches the distinct nanofiber deposition regions on the foil. When only a few jets are present, the nanofibers accumulate in a linear arrangement, for example (a) 3 jets and (b) 5 jets, reflecting the shortest path from the plate edge to the collector. When >~6 jets are present (c−f), neighboring jets deflect upward or downward to minimize interjet interactions. The scale is the same for all images, as indicated in Figure 8c. See also Figure 10 for jet deflection image.
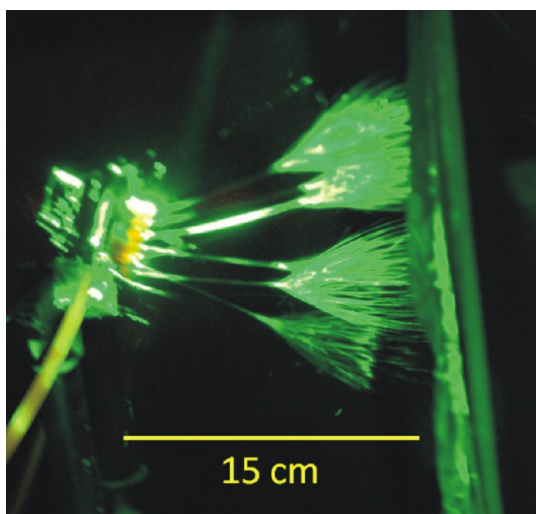
Figure 10. Optical image of plate edge electrospinning with multiple parallel jets as viewed from a side perspective. When sufficient numbers of instabilities are present, the jets deflect in the vertical dimension, both above and below the centerline directly between the source plate edge and the grounded collector.

geometry at the characteristic applied voltage level), the feed rate is approximately 5−6 μL/min, and the respective fiber diameters are consistently similar as 250 ± 20, 250 ± 25, and 230 ± 30 nm.

The observation of the same fiber quality from dramatically different configurations supports the assertion that unconfined geometries for electrospinning can efficaciously produce small diameter nanofibers, with the potential of a scaled-up fabrication rate due to the presence of many parallel jets.

4. CONCLUSION

High quality nanofibers were fabricated via edge electro-spinning from a remarkable simple apparatus consisting of a film of polymer fluid on a thin metal plate. The number of

fiber-forming jets is limited by the interplay between surface tension and the applied electric field up to a characteristic jet spacing (∼1.4 cm for the solutions utilized here) and voltage level, above which the repulsive electrostatic interactions between neighboring jets control the minimum jet spacing. Increases in the electric field amplitude provide more energy to overcome the cost of increasing the surface area of the fluid, and thus, applied voltage level increase is associated with more jets and higher jet density, if considering only surface tension effects. In contrast, once a sufficiently high applied voltage level is reached, where interjet interactions are the primary constraint on jet density, further raising the voltage increases the surface charge density on the fluid and thus worsens jet-to-jet interactions. Above this crossover level, the number of stable jets decreases as jet compression due to interjet electrostatic forces results in jet pinch-off and loss. Thus, the maximum number of jets (or, equivalently, the highest jet density) will occur as a balance between surface tension and jet-to-jet effects. Hence, naively increasing the source plate applied voltage level will not result in greater jet number.

Raising the applied voltage level also increases flow through each jet and thus can be associated with low quality (i.e., large diameter) fibers due to overfeeding of the fiber-forming jet. Our data illustrate a useful feature of jet-to-jet interactions near the crossover point at maximum stable jet number; the interactions compress the cone-jet size and limit increases in feed rate. With this compression, the edge electrospinning process is able to fabricate narrow-diameter, high quality nanofibers at the maximum jet number instead of requiring a lower applied voltage (resulting in fewer nanofiber forming jets) in order to obtain an appropriate flow rate. As part of this discussion, we illustrated the connection between cone-jet size and flow rate and showed that cone-jet size is proportional to the maximum velocity of the fluid through the jet, rather than being determined by the gravity or electrostatic capillary lengths.

Finally, the linear geometry of a plate edge employed here enabled jets to self-reorganize by deflecting in the vertical

direction (upward or downward away from the line connecting the plate and the center of the collector), which served to decrease the jet-to-jet interactions and create a two-dimensional array of nanofibers from a one-dimensional source. From an electrospinning perspective, the working distance (the length of the path from source jet to collector) is also slightly longer for the deflected jets, without a loss in the maximum electric field at the plate edge. In other words, the forming nanofiber has a longer distance over which to thin (by solvent evaporation and the whipping instability) before reaching the collector. Thus, this effect will maintain or even improve nanofiber quality.

■ AUTHOR INFORMATION

Corresponding Author
*E-mail: liclarke@ncsu.edu (L.I.C.).

Notes
The authors declare no competing financial interest.

■ ACKNOWLEDGMENTS

■ REFERENCES

(1) Lu, X. F.; Wang, C.; Wei, Y. *Small* **2009**, *5* (21), 2349−2370.
(2) Barhate, R. S.; Ramakrishna, S. *J. Membr. Sci.* **2007**, *296* (1−2), 1−8.
(3) Desai, K.; Kit, K.; Li, J. J.; Davidson, P. M.; Zivanovic, S.; Meyer, H. *Polymer* **2009**, *50* (15), 3661−3669.
(4) Heikkila, P.; Taipale, A.; Lehtimaki, M.; Harlin, A. *Polym. Eng. Sci.* **2008**, *48* (6), 1168−1176.
(5) Sambaer, W.; Zatloukal, M.; Kimmer, D. *Chem. Eng. Sci.* **2011**, *66* (4), 613−623.
(6) Thavasi, V.; Singh, G.; Ramakrishna, S. *Energy Environ. Sci.* **2008**, *1* (2), 205−221.
(7) Cavaliere, S.; Subianto, S.; Savych, I.; Jones, D. J.; Roziere, J. *Energy Environ. Sci.* **2011**, *4* (12), 4761−4785.
(8) Formo, E.; Lee, E.; Campbell, D.; Xia, Y. N. *Nano Lett.* **2008**, *8* (2), 668−672.
(9) Liang, D.; Hsiao, B. S.; Chu, B. *Adv. Drug Delivery Rev.* **2007**, *59* (14), 1392−1412.
(10) Goldberg, M.; Langer, R.; Jia, X. Q. *J. Biomater. Sci., Polym. Ed.* **2007**, *18* (3), 241−268.
(11) Kenawy, E. R.; Bowlin, G. L.; Mansfield, K.; Layman, J.; Simpson, D. G.; Sanders, E. H.; Wnek, G. E. *J. Controlled Release* **2002**, *81* (1−2), 57−64.
(12) Sill, T. J.; von Recum, H. A. *Biomaterials* **2008**, *29* (13), 1989−2006.
(13) Khil, M. S.; Cha, D. I.; Kim, H. Y.; Kim, I. S.; Bhattarai, N. *J. Biomed. Mater. Res., Part B* **2003**, *67B* (2), 675−679.
(14) Ma, Z. W.; Kotaki, M.; Inai, R.; Ramakrishna, S. *Tissue Eng.* **2005**, *11* (1−2), 101−109.
(15) McCullen, S. D.; Ramaswamy, S.; Clarke, L. I.; Gorga, R. E. *Wiley Interdiscip. Rev.: Nanomed. Nanobiotechnol.* **2009**, *1*, 369.
(16) Huang, Z. M.; Zhang, Y. Z.; Kotaki, M.; Ramakrishna, S. *Compos. Sci. Technol.* **2003**, *63* (15), 2223−2253.
(17) Stone, D. A.; Korley, L. T. J. *Macromolecules* **2010**, *43* (22), 9217−9226.
(18) Reneker, D. H.; Yarin, A. L.; Zussman, E.; Xu, H. Electrospinning of nanofibers from polymer solutions and melts. In *Advances in Applied Mechanics*; Aref, H., Van Der Giessen, E., Eds.; Elsevier Academic Press Inc.: San Diego, CA, 2007; Vol. *41*, pp 43−195.

(19) Luo, C. J.; Stoyanov, S. D.; Stride, E.; Pelan, E.; Edirisinghe, M. *Chem. Soc. Rev.* **2012**, *41* (13), 4708−4735.
(20) Thoppey, N. M.; Bochinski, J. R.; Clarke, L. I.; Gorga, R. E. *Polymer* **2010**, *51*, 4928.
(21) Thoppey, N. M.; Bochinski, J. R.; Clarke, L. I.; Gorga, R. E. *Nanotechnology* **2011**, *22* (34), 11.
(22) Thoppey, N. M.; Gorga, R. E.; Bochinski, J. R.; Clarke, L. I. *Macromolecules* **2012**, *45* (16), 6527−6537.
(23) Cengiz, F.; Dao, T. A.; Jirsak, O. *Polym. Eng. Sci.* **2010**, *50* (5), 936−943.
(24) Cengiz, F.; Jirsak, O. *Fibers Polym.* **2009**, *10* (2), 177−184.
(25) Lukas, D.; Sarkar, A.; Pokorny, P. *J. Appl. Phys.* **2008**, *103* (8), 7.
(26) Miloh, T.; Spivak, B.; Yarin, A. L. *J. Appl. Phys.* **2009**, *106* (11), 8.
(27) Niu, H. T.; Lin, T. *J. Nanomater.* **2012**, 725950.
(28) Niu, H. T.; Lin, T.; Wang, X. G. *J. Appl. Polym. Sci.* **2009**, *114* (6), 3524−3530.
(29) Niu, H. T.; Wang, X. G.; Lin, T. *J. Text. Inst.* **2012**, *103* (7), 787−794.
(30) Yarin, A. L.; Zussman, E. *Polymer* **2004**, *45* (9), 2977−2980.
(31) YenerF.; Jirsak, O. *J. Nanomater.* **2012**, 839317.
(32) Craster, R. V.; Matar, O. K. *Rev. Mod. Phys.* **2009**, *81* (3), 1131−1198.
(33) Olabisi, O. *Handbook of Thermoplastics*; Marcel Dekker: New York, 1997; p 581.
(34) Maity, S.; Downen, L. N.; Bochinski, J. R.; Clarke, L. I. *Polymer* **2011**, *52* (7), 1674−1685.
(35) McCullen, S. D.; Stano, K. L.; Stevens, D. R.; Roberts, W. A.; Monteiro-Riviere, N. A.; Clarke, L. I.; Gorga, R. E. *J. Appl. Polym. Sci.* **2007**, *105* (3), 1668−1678.
(36) McCullen, S. D.; Stevens, D. R.; Roberts, W. A.; Clarke, L. I.; Bernacki, S. H.; Gorga, R. E.; Loboa, E. G. *Int. J. Nanomed.* **2007**, *2* (2), 253−263.
(37) McCullen, S. D.; Stevens, D. R.; Roberts, W. A.; Ojha, S. S.; Clarke, L. I.; Gorga, R. E. *Macromolecules* **2007**, *40* (4), 997−1003.
(38) Ojha, S. S.; Afshari, M.; Kotek, R.; Gorga, R. E. *J. Appl. Polym. Sci.* **2008**, *108* (1), 308−319.
(39) Ojha, S. S.; Stevens, D. R.; Hoffman, T. J.; Stano, K.; Klossner, R.; Scott, M. C.; Krause, W.; Clarke, L. I.; Gorga, R. E. *Biomacromolecules* **2008**, *9* (9), 2523−2529.
(40) Ojha, S. S.; Stevens, D. R.; Stano, K.; Hoffman, T.; Clarke, L. I.; Gorga, R. E. *Macromolecules* **2008**, *41* (7), 2509−2513.
(41) Ramaswamy, S.; Clarke, L. I.; Gorga, R. E. *Polymer* **2011**, *52* (14), 3183−3189.
(42) de la Mora, J. F. The fluid dynamics of Taylor cones. In *Annual Review of Fluid Mechanics*; Annual Reviews: Palo Alto, CA, 2007; Vol. *39*, pp 217−243.
(43) de Gennes, P.-G.; Brochard-Wyart, F.; Quere, D. *Capillarity and Wetting Phenomena*; Springer: New York, 2010.
(44) Higuera, F. J. *Phys. Rev. E* **2008**, *78* (1), 11.